applied sciences

MDPI

Article

Multi-Hazard Exposure Prioritization with Time-Varying Population: Integrating Seismic Amplification Susceptibility and Flood Hazards in Seoul

Youngsuk Lee * and Jihye Kim

Disaster Management Research Center, The Seoul Institute, 57 Nambusunhwan-ro, 340-gil Seocho-gu, Seoul 06756, Republic of Korea; jihyek@si.re.kr
* Correspondence: ianlee@si.re.kr

Abstract

Urban disaster management frequently relies on isolated single-hazard assessments and static census data. This conventional approach systematically obscures the highly dynamic, time-varying nature of population exposure to co-located environmental hazards. This study develops an observation-based, time-adaptive multi-hazard exposure prioritization framework to quantify these spatiotemporal variations. We integrate seismic amplification susceptibility, derived from shear-wave velocity estimates, and empirical pluvial flooding footprints with hourly dynamic living population data at a 250 m grid resolution in Seoul, South Korea. Results indicate that multi-hazard integration refines spatial prioritization, with 11% of high-priority areas diverging from single-hazard models, primarily driven by highly amplifiable alluvial deposits. Furthermore, dynamic living population data revealed clear diurnal exposure shifts. Business districts exhibited a daytime-to-nighttime exposure ratio of 3.35, whereas residential areas showed an inverse ratio of 0.69, demonstrating that identical physical conditions generate markedly different exposure patterns depending on the daily urban rhythm. Based on these temporal dynamics, we classified high-priority zones into Persistent (79.4%), Day-peak (10.3%), and Night-peak (10.3%) transition types. These findings suggest that urban exposure must be managed as a time-varying attribute rather than a static feature. The proposed classification supports targeted mitigation: structural improvements for Persistent areas, dynamic crowd management for Day-peak zones, and localized alerts for Night-peak zones. Driven by globally accessible mobile data, this framework provides a transferable foundation for exposure-informed urban resilience planning across diverse metropolitan environments.

Keywords: multi-hazard; exposure assessment; dynamic population; spatiotemporal analysis; time-adaptive management; urban resilience

Check for updates

Academic Editors: Nicholas Vassiliou Sarlis and Michele D'Amato

Received: 6 February 2026
Revised: 1 April 2026
Accepted: 2 April 2026
Published: 3 April 2026

Copyright: © 2026 by the authors. Licensee MDPI, Basel, Switzerland. This article is an open access article distributed under the terms and conditions of the Creative Commons Attribution (CC BY) license.

1. Introduction

Urban areas increasingly face compound risks from multiple natural hazards under changing climatic conditions [1]. In high-density metropolitan environments, disaster risk often involves more than a single hazard [2]. Such hazards often intersect in space or time, creating compounded exposure patterns shaped by urban structure and population distribution [3]. Recent catastrophic events, such as the 2023 Türkiye–Syria earthquake sequence [4], the 2021 Zhengzhou flood in China [5], and the severe 2021–2023 floods across Western Europe and Italy [6], illustrate that densely populated urban centers remain highly

susceptible to compound and cascading hazards that exceed single-hazard frameworks, resulting in significant human and economic losses.

Among various compound risks, the co-occurrence of earthquakes and floods is particularly relevant in cities [7]. Floods occur recurrently and leave persistent spatial imprints [8], while earthquakes, although less frequent, can induce substantial functional disruption even at moderate magnitudes [9]. Seismic events can intensify flood hazards through ground subsidence, liquefaction, and damage to drainage infrastructure [10,11], increasing flood severity during subsequent rainfall events [12]. Consequently, earthquakes and floods often affect overlapping urban spaces shaped by geological and infrastructural conditions, especially in low-lying alluvial areas.

Despite this complexity, disaster management frameworks predominantly rely on single-hazard approaches [13,14], which account for nearly 88% of current disaster risk indicators [15]. While recent studies have shifted toward integrated multi-hazard frameworks, many approaches remain limited by oversimplified, deterministic overlay methods [16]. Such methodologies [2] primarily quantify spatial co-occurrence and treat hazard interactions as binary rather than continuous, which may not fully capture gradational exposure intensities.

Furthermore, the representation of population exposure remains a critical limitation. Most existing assessments utilize static demographic datasets, such as census or registered residential counts [17–22]. These metrics reflect nighttime conditions and fail to capture the daytime population variability driven by commuting and economic activities [23,24]. While Zhu et al. [25] effectively incorporated daytime–nighttime population fluctuations, their analysis was confined to a single-hazard context. Conversely, Depietri et al. [26] achieved a fine spatial resolution (30 m) in a multi-hazard framework via dasymetric mapping, but their reliance on census data meant the exposure representation remained fundamentally static. Consequently, there is a need to integrate continuous, multi-hazard proxies with high-resolution, time-varying population data.

Seoul, one of the most densely populated metropolitan areas in East Asia, faces both recurrent extreme rainfall events, which account for 60.7% of the national natural disaster economic losses between 2015 and 2024 [27], and low-probability but potentially high-impact seismic risk associated with site amplification in basin-type alluvial deposits [28,29]. The combined hazard characteristics and diurnal population variability make the city a relevant case for multi-hazard exposure assessment.

This study presents an observation-based multi-hazard exposure framework that shifts the focus from static spatial overlays to dynamic spatiotemporal prioritization. Based on the UNDRR (United Nations Office for Disaster Risk Reduction) disaster risk framework [30], which defines Risk as Hazard $\times$ Exposure $\times$ Vulnerability, this analysis specifically targets the hazard–exposure intersection. By integrating continuous physical hazard proxies with dynamic living population data, the framework evaluates relative exposure priority rather than absolute risk. To provide an empirical basis for urban resilience, this study aims to: (1) identify areas of overlapping seismic and flood hazards, (2) examine diurnal variations in population exposure, and (3) delineate high-resolution spatiotemporal priority zones based on the co-location of hazards and human presence.

2. Study Area and Data

2.1. Study Area

Seoul, the capital of South Korea, is a high-density metropolis in the central Korean Peninsula, covering approximately 605.21 km^2 (Figure 1a). Based on a Digital Elevation Model (DEM), the terrestrial elevations range from approximately 0 m to 826 m. Adminis-

tratively, Seoul comprises 25 autonomous districts (Gu, representing primary municipal divisions) (Figure 1b).

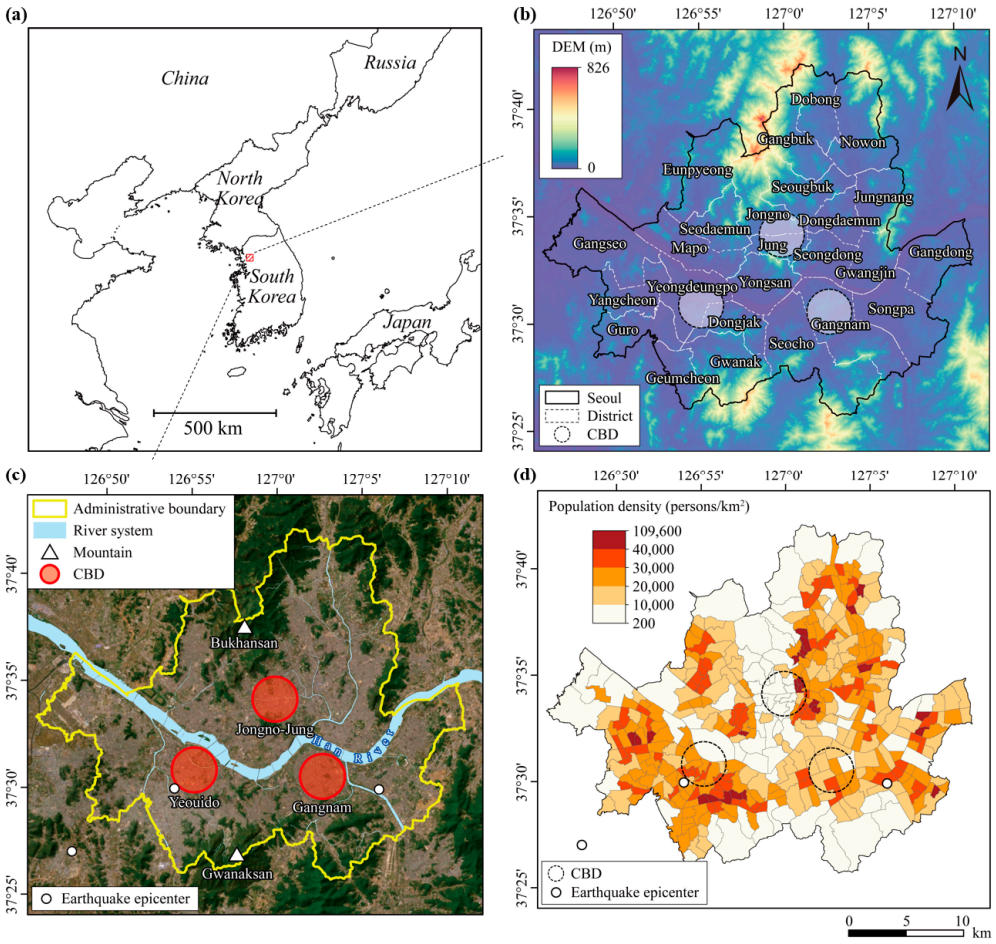


Figure 1. Study area overview of Seoul, South Korea: (**a**) location within the Korean Peninsula, (**b**) topographic variations with district boundaries from DEM, (**c**) satellite imagery showing the Han River, major mountain peaks, and the three CBDs, and (**d**) spatial distribution of registered population density by sub-district (Dong) in 2024.

The city features a basin topography, surrounded by mountainous terrain to the north (Bukhansan) and south (Gwanaksan) (Figure 1c). Alluvial plains and lowlands are distributed along the Han River and its tributaries. This topographic structure results in a heterogeneous distribution of river-adjacent areas and localized low-elevation zones within the urban core [31,32]. The city exhibits distinct functional zoning, with business and commercial activities heavily concentrated in three central business districts (CBDs): Jongno-Jung, Yeouido, and Gangnam [33].

As of September 2024, based on resident registration statistics [34], Seoul has a population of approximately 9.5 million across these 25 districts, which are further subdivided into 426 sub-districts (Dong, representing neighborhood-level administrative units) (Figure 1d). The registered population density shows a clear concentration in residential areas outside the CBDs. This urban structure drives substantial spatiotemporal variations in population distribution [8,35], with the same spatial unit exhibiting different exposure characteristics between daytime and nighttime [25].

Although the Korean Peninsula is traditionally classified as a region of low-to-moderate seismicity [36], a series of inland earthquakes with local magnitudes (M_L) exceeding 5.0, including the 2016 Gyeongju earthquake (M_L 5.8, hereafter GJ) and the 2017 Pohang earthquake (M_L 5.4, hereafter PH), has raised concerns regarding seismic risks

in Seoul [37,38] (Figure 2a). 2360 earthquakes were recorded across the Korean Peninsula between 1978 and 2024. Among these records, 157 events occurred within a 100-km radius of Seoul, yielding an annual average of 3.3 events. The majority of these localized events were micro-earthquakes; 79% registered magnitudes between M_L 2.0 and 3.0. Within the study area (Figure 2b), seismic activity has been restricted to infrequent, small-magnitude events, such as those near Songpa (M_L 2.3, 1990) and Yeongdeungpo (M_L 2.5, 2004). While Seoul has not experienced severe earthquake damage in recent history, the dense concentration of population, buildings, and critical infrastructure suggests that even moderate seismic events could result in considerable damage [32,39].

In contrast, urban flooding represents the most frequent and economically disruptive natural hazard in Seoul [8]. Historically, over 90% of property losses from natural disasters have been attributed to typhoons and heavy rainfall [27]. The spatial distribution of flood trace records reveals clear clustering in low-lying urban basins, particularly across the southern districts of Seoul (Figure 2b). Unlike the sparse seismic record, flood occurrences in Seoul are highly frequent yet temporally episodic. During the 15-year observation period (2010–2024), a cumulative total of 41,980 flood incidents were recorded, averaging 2799 events annually. However, these incidents were disproportionately concentrated in extreme years. The three most active years (2010, 2011, and 2022) accounted for over 95% of all records, with 2022 alone contributing 47% (19,881 incidents) of the total occurrences (Figure 2c). The 2022 extreme rainfall event, characterized by maximum hourly precipitation exceeding 141.5 mm, triggered severe inundation and casualties across the city's low-lying areas [40]. Specifically, more than 99% of these historical incidents were driven by pluvial factors, such as surface inundation and drainage capacity exceedance, with fluvial overflow accounting for merely 0.3% [41]. Recently, flood damage patterns have been dominated by short-duration, high-intensity rainfall events exacerbated by climate variability [42].

Seoul, therefore, serves as a representative metropolitan environment where low-frequency but high-impact seismic hazards intersect with recurrent pluvial flooding risks. The strong temporal variability in population distribution also makes the city an optimal case study for examining multi-hazard exposure patterns that static frameworks cannot adequately capture.

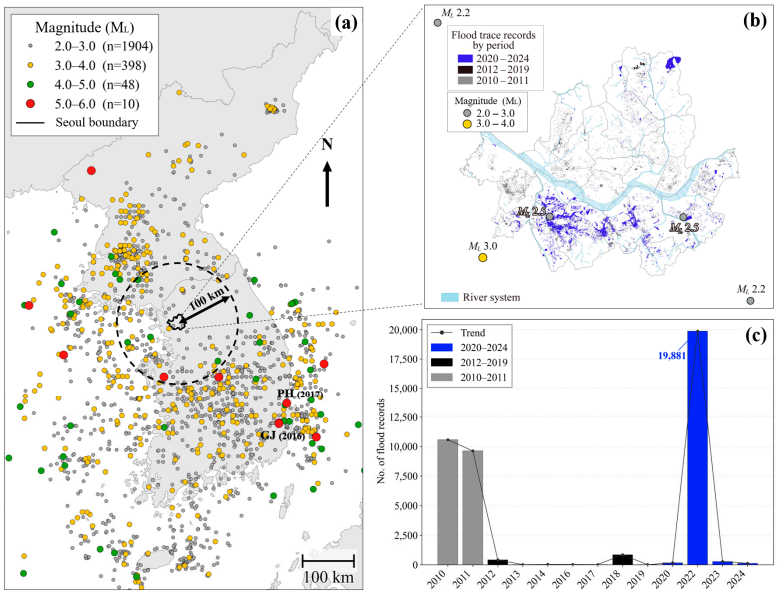


Figure 2. Natural hazard background of the study area: (**a**) spatial distribution of earthquakes across the Korean Peninsula (1978–2024) [43], (**b**) enlarged view of Seoul showing historical flood trace records by period and nearby earthquakes and (**c**) annual flood incident counts (2010–2024) [41].

2.2. Data Overview

The datasets include geotechnical borehole data, flood trace maps, and dynamic living population data. Data sources, including specific record counts, temporal coverage, spatial resolution, and data providers, are summarized in Table 1.

2.2.1. Geotechnical Borehole Data

Geotechnical borehole data provide direct physical characterizations of subsurface stratigraphy and soil engineering properties, which are essential for site-specific seismic assessments [44]. This study utilized a comprehensive dataset comprising 22,499 site investigation records obtained from the National Geotechnical Information Database System [45] across Seoul, covering a temporal scope from 2003 to 2018 (Figure 3a). Specifically, the dataset provides stratigraphic descriptions (e.g., soil type and layer thickness) at 22,499 locations, Standard Penetration Test (SPT) N-values at 13,054 locations, and in situ shear-wave velocity (V_S) measurements at 515 locations. The N-value represents the number of blows required to drive a sampler 30 cm into the ground, serving as a primary empirical indicator of local soil stiffness and density. Additionally, in situ V_S measurements capture the propagation speed of seismic waves, which is the fundamental parameter for evaluating site-specific seismic amplification [46]. These data provide essential inputs for characterizing seismic amplification susceptibility (e.g., V_{S30}) based on local geotechnical conditions [47,48].

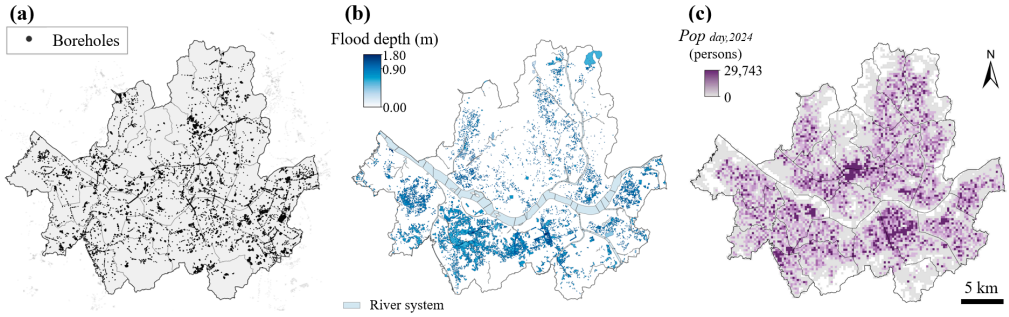


Figure 3. Spatial distribution of primary datasets used in this study: (**a**) geotechnical boreholes locations (2003–2018); (**b**) historical flood depth records (2010–2024); and (**c**) average daytime dynamic living population (2024).

2.2.2. Flood Trace Maps

Flood trace maps are observation-based datasets documenting the spatial extent, location, and depth of inundation from post-event field surveys and administrative records over a 15-year period (2010–2024). Compiled by the Seoul Metropolitan Government [41], the archive comprises 41,980 spatial polygon records (Figure 3b). Because they document the physical manifestation of flooding that actually occurred, these records inherently integrate both pluvial and fluvial mechanisms, providing an empirical representation of persistent flood hazard.

The dataset consists of two primary types of spatial information. First, the spatial extent layers define "where and how much" the area was flooded, providing critical attributes such as inundation depth and affected area. Second, the event-specific layers detail "when and why," recording the flood causes, event duration, and year.

Ultimately, these observation-based maps provide a reliable empirical record of persistent flood hazards within the urban environment, including residual hazards after structural mitigation implementation [49].

2.2.3. Dynamic Living Population Data

This study employed dynamic living population data derived from mobile communication records to quantify time-specific population exposure [50]. The overall time-averaged spatial distribution of this dataset reveals a pronounced concentration within the city's three major CBDs (Figure 3c). These data represent populations present and active within a given space at specific times, functioning as a de facto population proxy for time-varying urban exposure. Although the dataset represents the population distribution in 2024, it serves as a proxy for the general functional population pattern of the urban space, as Seoul's core urban structure and land-use patterns have remained structurally stable.

As of 2024, South Korea's mobile phone ownership rate exceeds 98% of the total population [51], suggesting high representativeness of these data as a population proxy. To account for potential under-representation of non-users among vulnerable populations, the dataset utilizes an expansion and calibration algorithm that integrates mobile records with public administrative datasets, including resident registration and public transit data [52].

Data are provided on an hourly basis at a 250 m × 250 m grid resolution, including a total of 10,125 grid cells across the study area. This represents the finest available resolution for time-specific population data in Seoul.

Table 1. Overview of datasets used in the multi-hazard exposure prioritization framework.

Dataset	Spatial Resolution	Temporal Scope	Key Attributes	Source
Geotechnical borehole data	point	2003–2018	stratigraphy, SPT N-values, shear-wave velocity	National Geotechnical Information Database System [45]
Flood trace maps	vector (polygon)	2010–2024	flood depth, area, causes, event year	Seoul Open Data Plaza [41]
Dynamic living population	250 m × 250 m grid	2024	time-specific population (00 h–23 h)	Seoul Open Data Plaza [50]

3. Methodology

3.1. Multi-Hazard Exposure Prioritization Framework

This study adopts the international disaster risk framework [30], where disaster risk (R) is expressed as a function of hazard, exposure, and vulnerability: $R = f(H, E, V)$. Hazard (H) represents potentially hazardous physical phenomena, exposure (E) denotes populations or assets located in hazard-prone areas, and vulnerability (V) represents susceptibility to hazard impacts. Our framework integrates two hazard proxies with time-varying population exposure, but does not incorporate spatially explicit vulnerability indicators (e.g., building fragility or demographic susceptibility). Because comprehensive micro-spatial vulnerability data are often unavailable or inconsistent across metropolitan scales [53], labeling the integrated output as "risk" without the vulnerability component would be conceptually inconsistent with the standard framework. Therefore, this study adopts the term "exposure priority" to quantify the co-location of multiple hazards and dynamic human presence. This relative prioritization provides a practical basis for preliminary spatial screening and municipal resource allocation, instead of an absolute risk quantification.

Within this framework, the hazard component (H) is decomposed into two subcomponents: seismic amplification susceptibility (S_i) and flood hazard (F_i). Seismic site conditions are characterized by the time-averaged shear-wave velocity of the upper 30 m (V_{S30}), which serves as a proxy for local ground motion amplification propensity and is inversely scaled to derive S_i. Flood hazard is quantified through the temporally weighted cumulative inundation intensity (CI_i) derived from accumulated flood trace maps, which is subsequently normalized into the flood hazard index (F_i). The exposure component (E) is represented by time-specific dynamic living population counts ($Pop_{i,t}$), which are normalized into the time-varying population exposure index ($E_{i,t}$). Because explicit vulnerability (V) data are not integrated, this parameter is held constant (i.e., assumed spatially uniform). The framework thus evaluates conditional exposure priority—the spatial distribution of the exposed population given that an extreme event occurs—rather than absolute probabilistic risk. Accordingly, the hazard components are treated as temporally invariant spatial indicators, and the present analysis focuses on the contribution of hazard–exposure interactions to spatial exposure prioritization. This methodological scope is discussed as a limitation in Section 5.5.

The analysis consisted of four phases (Figure 4): (1) data preprocessing and standardization; (2) derivation of hazard and exposure components; (3) multi-hazard exposure priority integration; and (4) spatiotemporal priority analysis. The analytical workflow proceeds sequentially, with detailed methodologies for each phase presented in the subsequent sections.

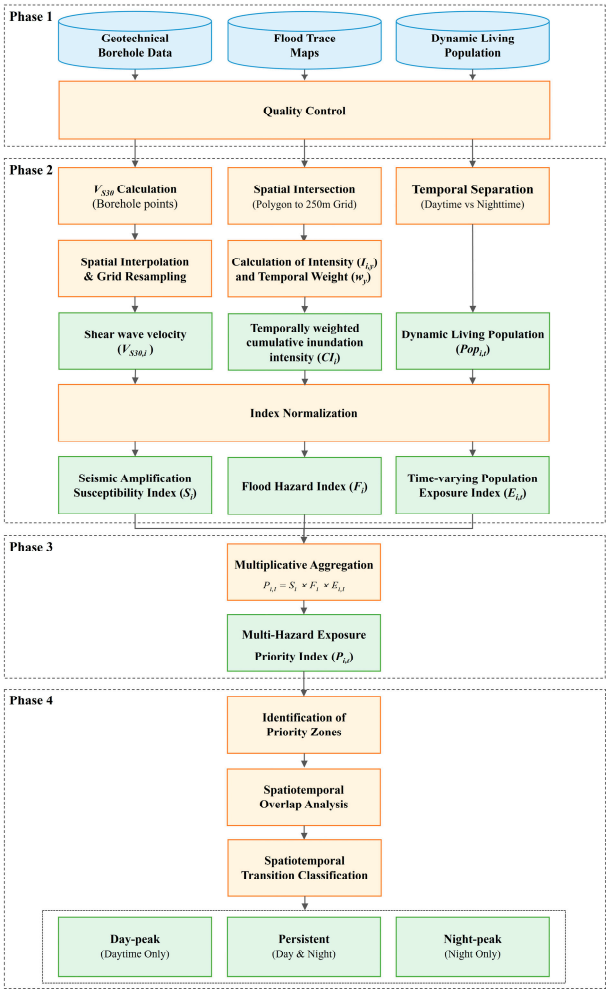


Figure 4. Conceptual framework of the multi-hazard exposure prioritization integrating seismic amplification susceptibility, flood hazard, and time-varying population exposure.

3.2. Data Pre-Processing and Spatial Standardization

All spatial datasets were subjected to quality control and coordinate unification to ensure analytical consistency. For the geotechnical data, boreholes with incomplete or inconsistent stratigraphic records were excluded following established screening procedures [44]. For the flood trace maps, geometry validity and attribute completeness of the polygons were systematically verified. The dynamic living population data, provided as pre-processed temporal grids, required no further outlier filtering. All spatial layers were subsequently projected to a unified national coordinate reference system (EPSG:5179).

To facilitate spatial integration, a unified 250 m × 250 m analysis grid was established, corresponding to the native resolution of the population exposure data.

3.3. Derivation of Hazard and Exposure Components

To enable the multiplicative integration of fundamentally different variables, each indicator was normalized using min-max transformation to dimensionless indices ranging from 0 to 1:

$$X_i^* = \frac{X_i - X_{min}}{X_{max} - X_{min}} \quad (1)$$

where X_i^* is the normalized index, X_i denotes the original value for grid cell i, and X_{min}, X_{max} represent the minimum and maximum values. The specific derivation of X_i for each component is described in the subsequent sections. For indicators negatively correlated with the hazard, a reverse min-max transformation was applied.

3.3.1. Seismic Amplification Susceptibility Component

Seismic amplification susceptibility was characterized through amplification propensity derived from subsurface geotechnical conditions. V_{S30}, was adopted as the representative indicator. V_{S30} represents the time-averaged shear-wave velocity of the upper 30 m and is widely used as a proxy for site amplification in seismic design framework [54]. This approach focuses on local site effects that modify ground motion rather than probabilistic seismic hazard or intensity modeling. Although V_{S30} may not capture all complexities of deep basin effects, it provides a standardized and spatially continuous metric suitable for grid-based multi-hazard integration.

V_{S30} Estimation

V_S profiles were developed using two approaches suggested by [44]. For boreholes with SPT measurements, V_S values were estimated from N-values using the empirical correlation proposed by Sun et al. [55].

$$V_S = 65.64 \times N^{0.407} (\mathrm{m/s}) \quad (2)$$

For boreholes lacking SPT data, representative V_S values were assigned using a simplified stratigraphic classification into seven soil and rock groups proposed by Lee, Lee and Park [44] (Table 2). These V_S values were derived from 515 available seismic survey measurements conducted across Seoul.

For each borehole, V_{S30} was calculated as:

$$V_{S30} = \frac{30}{\sum_{i=1}^{n} \frac{h_i}{V_{S,i}}} \quad (3)$$

where h_i and $V_{S,i}$ denote the thickness and shear-wave velocity of layer i. Spatial distribution of V_{S30} was estimated using ordinary kriging interpolation. Kriging was selected for its ability to provide unbiased predictions and quantify spatial uncertainty through prediction

variance. Cross-validation yielded RMSE = 189.85 m/s, corresponding to approximately 26% of the mean V_{S30}, indicating interpolation error within the range of observed spatial variability. Then to ensure spatial alignment with the population exposure data, the continuous V_{S30} surface was subsequently aggregated to the analysis grid by calculating the spatial mean within each cell.

Table 2. Representative V_S values for soil layers with reference correlations (adapted from Lee, Lee and Park [44]).

Type of Soil Layer	V_S (m/s)		
	Average	Standard Deviation	Coefficient of Variation
Fill	227	115	0.51
Sediment	278	201	0.72
Weathered soil	388	175	0.45
Weathered rock	605	219	0.36
Soft rock	924	343	0.37
Medium-hard rock	1273	303	0.24
Hard rock	1194	449	0.37

Seismic Amplification Susceptibility Index Derivation

Lower V_{S30} values correspond to softer materials that tend to amplify seismic ground motion. To align the indicator with the concept of hazard, where higher values represent greater site instability, V_{S30} was transformed into a seismic amplification susceptibility index (S_i) using reverse min-max normalization:

$$S_i = \frac{V_{S30,max} - V_{S30,i}}{V_{S30,max} - V_{S30,min}} \quad (4)$$

where $V_{S30,max}$ and $V_{S30,min}$ are the maximum and minimum shear-wave velocities across the study area. This linear transformation maps the minimum V_{S30} value to 1 and the maximum V_{S30} value to 0. By utilizing this reversed scale, the index directly reflects amplification propensity.

3.3.2. Flood Hazard Component

Flood hazard was characterized using accumulated flood trace maps. This approach focuses on the physical manifestation of urban flooding as empirically observed, rather than on simulated outputs derived from rainfall scenarios, hydrological models. By relying on observation-based records, the analysis captures locations with recurrent or persistent inundation exposure within the urban environment.

Grid-Based Flood Data Integration

To ensure spatial consistency with the unified analysis grid, the 41,980 vector-based flood trace polygons were integrated using a geometric intersection operation. When a flood polygon was fully contained within a single grid cell, its full geometry and depth attributes were retained directly. Polygons crossing grid boundaries were divided precisely along the grid lines.

For each resulting fragment generated by the intersection between flood event k and grid cell i, the exact inundated area ($A_{k,i}$) was calculated. The original inundation depth ($D_{k,i}$) of the source polygon was preserved and assigned to the corresponding grid cell. This area-preserving geometric allocation maintains the physical extent of the empirical flood records without spatial distortion, establishing the foundational inputs for the grid-level hazard index.

Flood Hazard Index Derivation

Flood hazard was quantified by calculating the temporally weighted cumulative intensity of observed inundation events. This cumulative approach inherently captures the frequency of flooding (i.e., areas with repeated events accumulate higher values), while an explicit weighting scheme accounts for the recency of the events.

The annual inundation intensity ($I_{i,y}$) for grid cell i in year y was defined as the cumulative magnitude of all events occurring within that year, calculated as:

$$I_{i,y} = \sum_{k=1}^{N_{i,y}} D_{k,i} \times A_{k,i} \quad (5)$$

where $D_{k,i}$ is the flood depth, $A_{k,i}$ is the inundated area of cell i during event k, and $N_{i,y}$ is the total number of events in cell i during year y.

To account for recency effects, a linear temporal weighting scheme was applied, assigning weights (w_y) from 0.1 (2010) to 1.0 (2024). The temporally weighted cumulative inundation intensity (CI_i) is calculated by accumulating these weighted annual intensities:

$$CI_i = \sum_{y=2010}^{2024} I_{i,y} \times w_y \quad (6)$$

These values were subsequently min-max normalized to derive the final Flood Hazard Index (F_i).

3.3.3. Time-Varying Population Exposure Component

Population exposure, P_t, was quantified using the hourly dynamic living population data to capture temporal exposure dynamics. To determine representative temporal states for the assessment, monthly, seasonal, and diurnal population distribution patterns were compared using the 2024 dataset. Monthly and seasonal variations in total population exposure were relatively small, with coefficients of variation of 0.6–0.8%, whereas the diurnal contrast reached approximately 18%, with daytime population being consistently higher than nighttime population throughout the year. Accordingly, representative temporal states were defined based on the day–night population distribution, while weekday and weekend conditions were analyzed separately.

The city-wide hourly population distributions exhibited clear diurnal patterns, reaching a peak during the afternoon due to commuting and commercial activities and dropping to a minimum during the early morning hours (Figure 5). On weekdays, the total population ranged from approximately 10.11 million at nighttime to 11.93 million during daytime, while weekend populations were lower than weekday populations by up to 0.33 million. Based on these hourly average curves (Figure 5), daytime (14:00) and nighttime (04:00) periods were defined to extract the representative population counts ($Pop_{i,t}$). These raw population counts ($Pop_{i,t}$) were subsequently min-max normalized to serve as the final time-varying population exposure index ($E_{i,t}$).

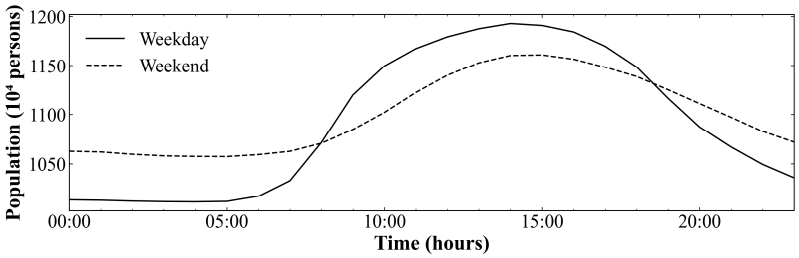


Figure 5. Hourly variation in dynamic living population in Seoul for weekdays and weekends (2024).

3.4. Multi-Hazard Exposure Priority Integration

The multi-hazard exposure priority index ($P_{i,t}$) was calculated by multiplying normalized hazard and exposure components:

$$P_{i,t} = S_i \times F_i \times E_{i,t} \quad (7)$$

where i and t indicate the grid cell and the time state, respectively.

This multiplicative structure emphasizes grid cells where seismic susceptibility, flood hazard, and population exposure are simultaneously high, while low values in any component reduce the overall metric. The resulting $P_{i,t}$ is therefore interpreted as a co-location-based exposure priority index, enabling comparative assessment of relative multi-hazard exposure intensity across space and time.

3.5. Spatiotemporal Priority Analysis

A spatiotemporal priority analysis was conducted to identify grid cells exhibiting elevated multi-hazard exposure priority under time-specific population conditions and to characterize temporal transitions in priority status.

3.5.1. Definition of Time-Specific Priority Zones

For each time period, grid cells were ranked by P, and those within the top 5% of the distribution were classified as priority zones. This percentile-based approach provides a relative prioritization framework that does not rely on absolute priority thresholds. The 5% threshold was selected based on sensitivity analysis testing alternative values (top 3%, 7% and 10%), which confirmed robust spatial patterns across reasonable threshold variations. A spatial clustering analysis using the Getis–Ord Gi* statistic was additionally conducted to verify the spatial coherence of the percentile-defined priority zones. Priority zones were delineated separately for daytime and nighttime periods and analyzed independently for weekdays and weekends.

3.5.2. Classification of Spatiotemporal Transition Types

Based on the overlap of daytime and nighttime priority zones, grid cells were classified into four transition types:

(i) Persistent: High-priority during both daytime and nighttime,
(ii) Day-peak: High-priority only during daytime,
(iii) Night-peak: High-priority only during nighttime,
(iv) Non-priority: Not classified as high-priority in either period.

This classification framework efficiently captures the temporal heterogeneity in the multi-hazard exposure priority index, distinguishing areas with stable priority (Persistent) from those whose importance shifts with time-dependent population dynamics (Day-peak, Night-peak).

3.5.3. Exposure Difference Calculation

An exposure difference analysis was performed by aggregating the dynamic living population counts for each transition type and time period. The quantitative differences between daytime and nighttime exposure were calculated to evaluate the temporal variation and identify the magnitude of the exposed population shifting within these dynamic priority zones.

4. Results

4.1. Spatial Distribution of Hazard Components

4.1.1. Seismic Amplification Susceptibility Index

The spatial distribution of V_{S30} exhibited a continuous gradient across the study area (Figure 6a). High V_{S30} values were prominently observed in the mountainous areas, while lower values were predominantly distributed along the Han River corridor and its major tributaries. Statistically, the V_{S30} distribution showed substantial heterogeneity (Figure 6b). Values ranged widely from 228.5 to 1897 m/s, with a mean of 717 m/s and a median of 627 m/s, indicating the coexistence of soft alluvial deposits and stiff bedrock conditions. Following the reverse min-max normalization, the resulting S_i mirrored this spatial pattern in reverse. Higher index values, which represent greater amplification susceptibility, were heavily concentrated in the low-lying areas and river corridors characterized by lower V_{S30} values.

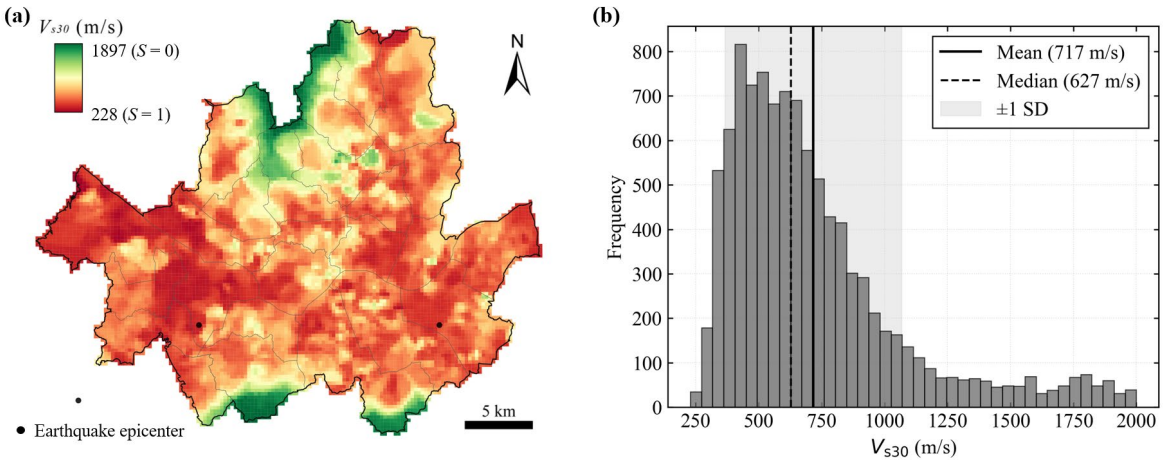


Figure 6. Spatial and statistical distribution of V_{S30} derived from geotechnical borehole data: (**a**) spatial map estimated by ordinary kriging interpolation (RMSE = 189.85 m/s), where lower values indicate higher S; and (**b**) histogram of the value distribution (mean = 717 m/s, median = 627 m/s, range = 228.5–1897 m/s).

4.1.2. Flood Hazard Index

The spatial distribution of CI_i and its corresponding normalized index F exhibited pronounced spatial heterogeneity, with uneven clustering of high values across the study area (Figure 7a). Elevated index values were concentrated in the southwestern sector, where repeated inundation events formed localized linear and clustered patterns adjacent to rivers and low-lying depressions. Areas experiencing severe flooding in recent years showed elevated index values even when historical frequency was moderate, reflecting the influence of recency weighting.

To assess the spatial consistency of this hazard metric, the CI_i values were aggregated to the district (Gu) scale to derive the cumulative index (CI_d^{sum}) and compared it against actual historical flood damage statistics recorded since 1995 (Figure 7b,c). The aggregated CI_d^{sum} exhibited statistically positive correlations with both cumulative economic losses ($r = 0.75$, $p < 0.001$) and reported casualties ($r = 0.55$, $p < 0.01$).

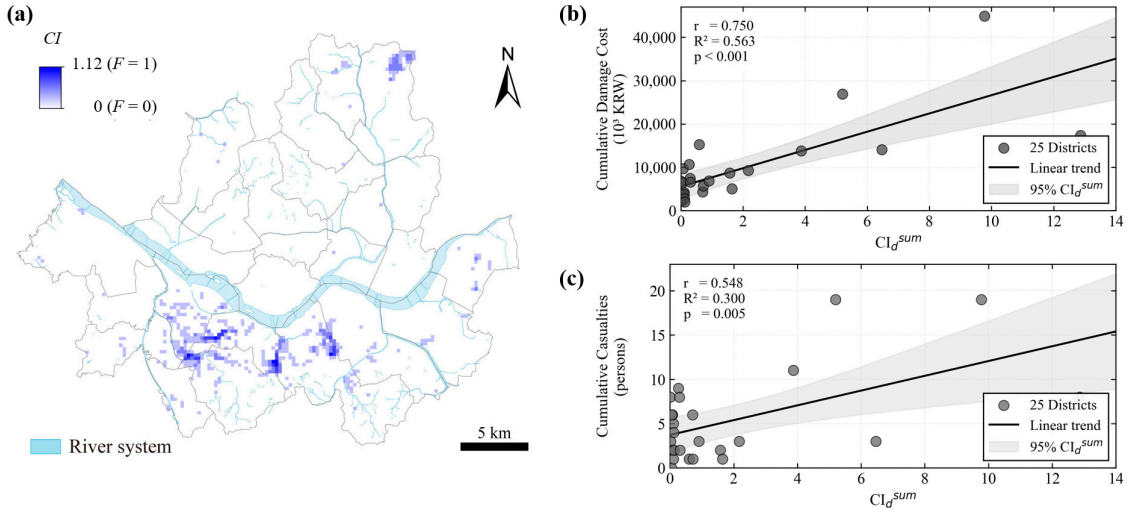


Figure 7. Derivation and validation of the flood hazard component: (**a**) spatial distribution of the grid-level *CI* and *F*, (**b**) correlation with cumulative economic damage, and (**c**) correlation with cumulative casualties based on historical records since 1995, with shaded regions indicating 95% confidence intervals.

4.1.3. Effect of Multi-Hazard Integration

The top 5% priority zones identified by the single-hazard (flood-only, *F*) and integrated multi-hazard (*S* and *F*) approaches showed substantial spatial overlap, with 89% of grid cells commonly identified by both models (Figure 8). This concordance indicates that flood hazard remains the dominant spatial driver of exposure priority in Seoul.

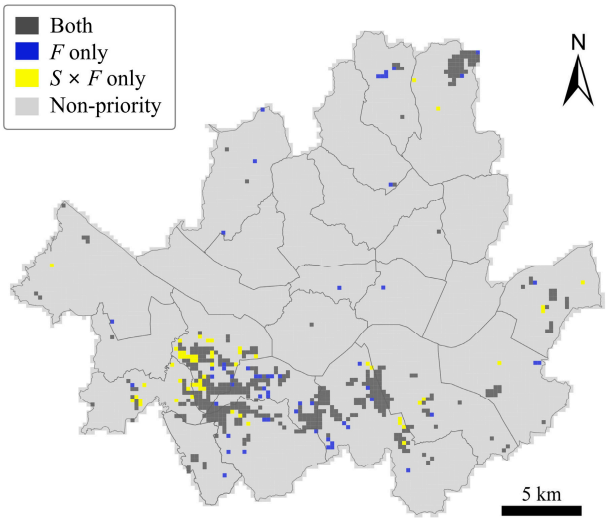


Figure 8. Spatial comparison of the top 5% priority zones identified by the single-hazard (flood-only, *F*) and the integrated multi-hazard (*S* and *F*) approaches.

However, 11% of priority zones (56 grid cells) diverged between the two approaches. While the flood hazard structure is inherently driven by low-lying areas prone to drainage capacity exceedance, the integration of seismic amplification susceptibility alters the spatial distribution of potential hazards. In particular, incorporating *S* increases the integrated priority in southwestern Seoul, where soft alluvial deposits and thicker sediments indicate higher amplification potential, thereby elevating areas that are not captured by the flood-only prioritization. This spatial discrepancy reveals the limitation of relying solely on single-hazard approaches in geologically diverse urban environments.

4.2. Spatial Distribution of Population Exposure

The dynamic living population showed clear temporal variation by time of day and day of week (Figure 5). Spatially, as shown in Figure 9, the weekday daytime population was heavily concentrated in CBDs, whereas the nighttime population was more evenly distributed toward residential areas. Weekend nighttime patterns closely resembled those of weekday nighttime, while the weekend daytime exhibited diminished concentration in the CBDs compared with weekdays. This spatiotemporal variation reflects daily commuting patterns and the functional differentiation of urban space.

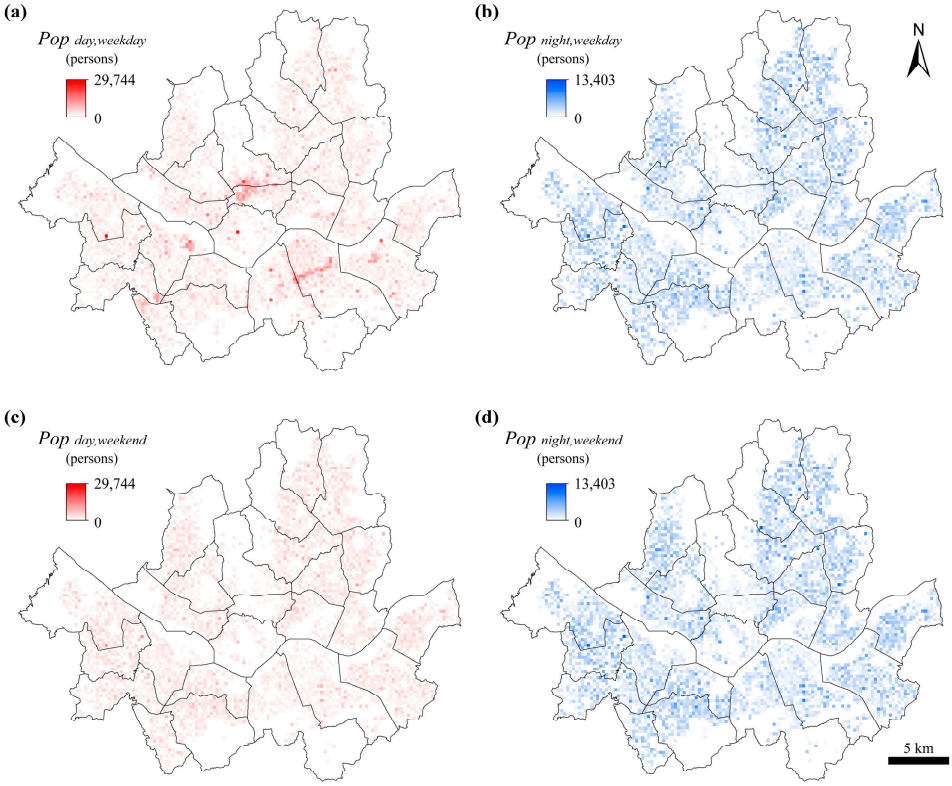


Figure 9. Spatial distribution of dynamic living population in Seoul: (**a**) weekday daytime (14:00), (**b**) weekday nighttime (04:00), (**c**) weekend daytime (14:00), and (**d**) weekend nighttime (04:00), with color scales unified separately for daytime (**a**,**c**) and nighttime (**b**,**d**) maps.

A comparison between the nighttime dynamic living population (Figure 9b,d) and the registered residential population density (Figure 1d) showed strong spatial consistency. This indicates the representativeness of mobile-based population data for accurately capturing time-varying exposure.

4.3. Integration of Multi-Hazard Exposure Priority

The multi-hazard exposure priority index exhibited distinct spatiotemporal heterogeneity between daytime and nighttime across both weekdays and weekends (Figure 10). During the weekday daytime (Figure 10a), the highest priority values were concentrated in major CBDs, including Yeongdeungpo, Gangnam, and Seocho (hereafter referred to as Zone A). Conversely, during the nighttime (Figure 10b), the spatial distribution of priority shifted and became more broadly dispersed, centering on residential districts such as Dongjak and Gwanak (hereafter referred to as Zone B). Weekend patterns maintained these general spatial tendencies (Figure 10c,d).

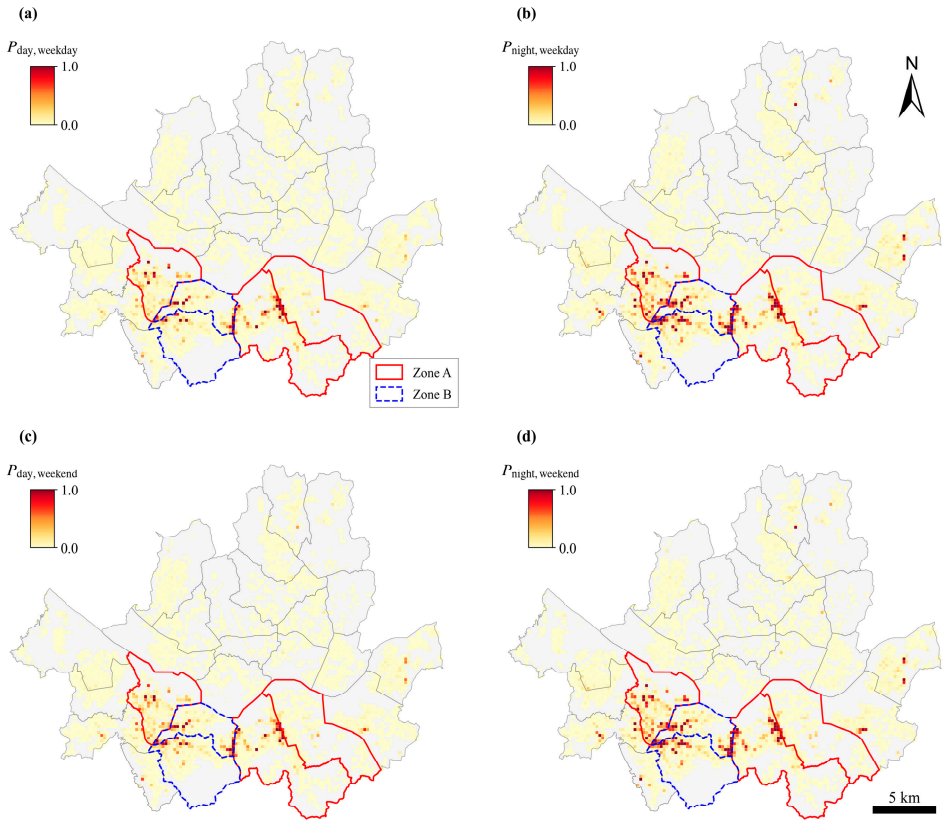


Figure 10. Spatial patterns of the multi-hazard exposure priority index in Seoul: (**a**) weekday daytime (14:00), (**b**) weekday nighttime (04:00), (**c**) weekend daytime (14:00), and (**d**) weekend nighttime (04:00), with Zone A (red solid line) and Zone B (blue dashed line) delineated in each panel.

To explicitly visualize the spatial asymmetry in diurnal exposure, the day–night priority difference (ΔPriority = Daytime − Nighttime) was mapped (Figure 11). While the majority of the grid cells (approximately 61%) remained temporally neutral ($\Delta Priority \approx 0$), distinct spatial clusters emerged at the distributional extremes. Specifically, the analysis identified structurally significant daytime-dominant clusters ($\Delta Priority > 0$) and nighttime-dominant clusters ($\Delta Priority < 0$). Within these localized extremes, the temporal amplification was substantial. In the daytime-dominant CBDs (Zone A), the daytime priority exceeded the nighttime priority by a factor of 2.48 on weekdays and 1.62 on weekends. In contrast, in the nighttime-dominant residential districts (Zone B), the nighttime priority was 2.02 times higher than the daytime priority on weekdays and 1.69 times higher on weekends. These pronounced diurnal variations indicate the limitation of static exposure assessments, providing the foundation for the high-resolution spatiotemporal transition classification detailed in Section 4.4.

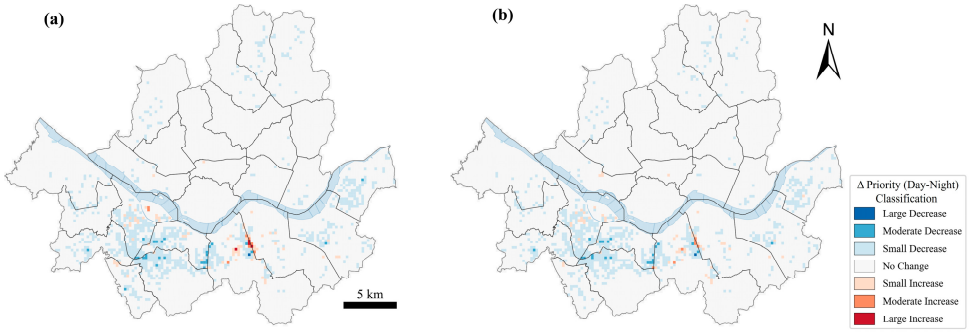


Figure 11. Day–night differences in the multi-hazard exposure priority index for (**a**) weekdays and (**b**) weekends.

4.4. Spatiotemporal Priority Patterns

4.4.1. Spatiotemporal Transition Types and Exposure Differences

Application of the top 5% percentile threshold identified high-priority grid cells based on multi-hazard exposure priority ranking for each time period, as summarized in Table 3. As illustrated in Figure 12, these priority zones were concentrated in business-oriented districts corresponding to Zone A and residential neighborhoods corresponding to Zone B. Priority zones formed contiguous spatial patterns rather than uniform dispersion and were aligned with major urban functional areas. A supplementary assessment using four representative seasonal weekdays further indicated that the main spatial configuration of these priority zones remained broadly consistent across the seasonal cases, with CBD-centered concentration and major urban corridors continuing to emerge as the dominant pattern (Figure A1).

Table 3. Population exposure characteristics by spatiotemporal transition type for weekdays and weekends.

Period	Transition Type	No. of Grid Cells	P_{Day}	P_{Night}	ΔP ($P_{Day} - P_{Night}$)	Ratio (P_{Day}/P_{Night})
Weekday	Persistent	449	1,339,989	1,142,509	197,480	1.17
	Day-peak	58	204,227	61,004	143,223	3.35
	Night-peak	58	114,618	167,034	−52,416	0.69
Weekend	Persistent	466	1,365,522	1,258,467	107,055	1.09
	Day-peak	41	108,613	42,252	66,361	2.57
	Night-peak	41	100,758	117,297	−16,539	0.86

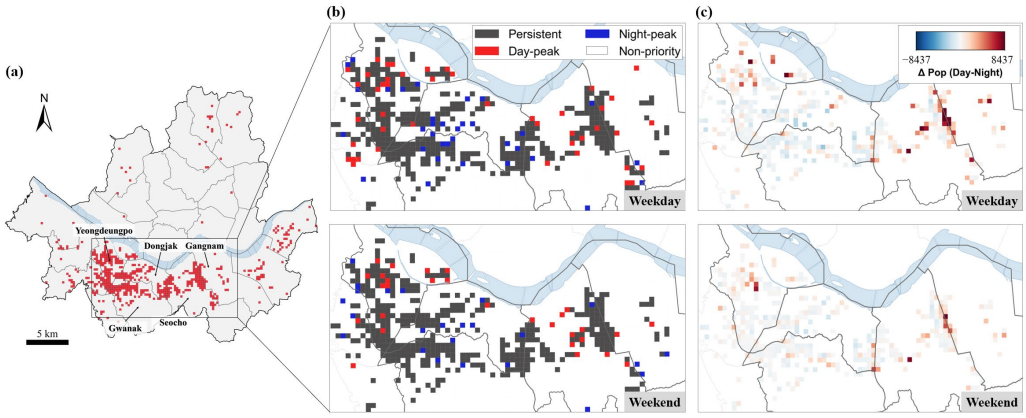


Figure 12. Spatiotemporal priority zone classification: (**a**) spatial distribution of the top 5% priority zones, (**b**) transition type classification (Persistent, Day-peak, Night-peak) for weekdays and weekends, and (**c**) day–night dynamic living population differences by zone type.

Based on the spatial overlap of daytime and nighttime priority zones, 565 weekday priority cells were classified into three transition types (Figure 12b). Persistent zones, representing continuously high-priority areas, accounted for 79.4% of all priority cells. However, the remaining dynamic zones, Day-peak (10.3%) and Night-peak (10.3%), revealed critical temporal shifts. The spatial distribution of these transition types showed distinct geographic divergence. Persistent zones were broadly distributed across both Zones A and B. In contrast, Day-peak zones were concentrated along business corridors, largely overlapping Zone A, while Night-peak zones were distributed across residential neighborhoods, largely overlapping Zone B. Weekend patterns demonstrated similar structural tendencies (Persistent: 85.0%, Day-peak: 7.5%, and Night-peak: 7.5%), with a slightly contracted dynamic range.

A quantitative analysis revealed substantial temporal asymmetries in population exposure across transition types, as summarized in Table 3 and illustrated in Figures 12 and 13. Persistent zones contained the largest absolute numbers of exposed population, maintaining approximately 1.34 million during weekday daytime and 1.14 million at nighttime. While this indicated a massive sustained exposure, the most dramatic temporal fluctuations were observed in the transient zones. Day-peak zones exhibited extreme daytime vulnerability; the exposed population increased from 61,004 at nighttime to 204,227 during the daytime, increasing by a factor of 3.35. Conversely, Night-peak zones showed an inverse exposure pattern, with the population increasing from 114,618 during the daytime to 167,034 at nighttime (day/night ratio = 0.69).

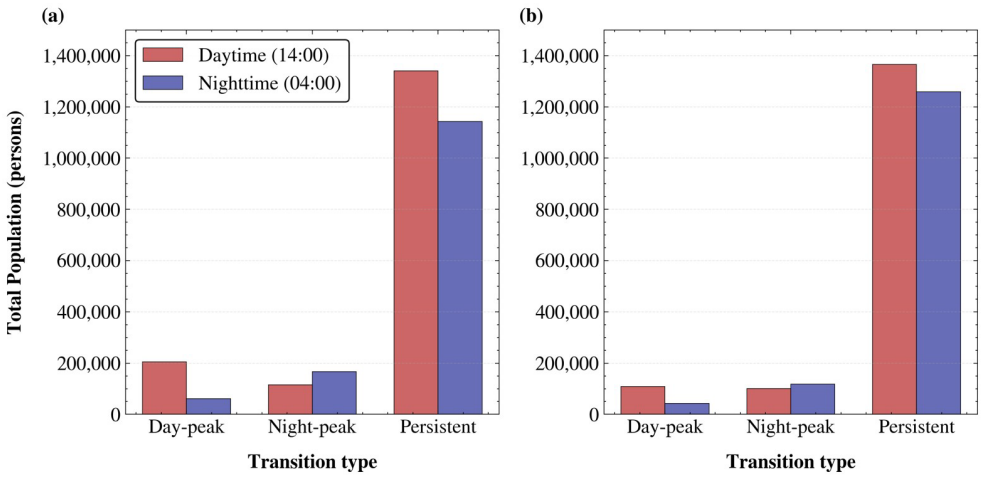


Figure 13. Total population exposure by spatiotemporal transition type for (**a**) weekdays and (**b**) weekends.

Weekend dynamics mirrored these trends but with moderated amplitudes due to reduced commuting flows; Day-peak zones still experienced an exposed population increase of 2.57 times, while Night-peak zones maintained a nighttime-dominant ratio of 0.86. These results indicate that exposure levels vary substantially across temporal transition types, suggesting that static census-based assessments may not fully capture the magnitude and direction of diurnal population redistribution in both business and residential districts.

4.4.2. Spatial Coherence and Threshold Sensitivity

A top 5% threshold was selected to define priority zones, capturing the highest levels of multi-hazard exposure while maintaining a manageable spatial extent for metropolitan-scale mitigation planning. To validate the robustness of this classification, a sensitivity analysis was conducted under weekday conditions across alternative thresholds (top 3%, 7%, and 10%), as detailed in Table 4. In this assessment, the dynamic transition types (Day-peak and Night-peak) were grouped as Temporal-only zones to evaluate the overall structural stability.

Table 4. Sensitivity analysis of priority zone classification under alternative percentile thresholds (weekday conditions).

Threshold	Priority Grids	Persistent (%)	Temporal-Only (%)	Pattern Concordance (%)
3%	353	72.2	27.8	97.1
5% (baseline)	565	79.4	20.5	—
7%	781	81.6	18.4	97.0
10%	1096	84.9	15.1	93.7

The analysis revealed that the spatial pattern of priority zones remained highly consistent. Pattern concordance with the 5% baseline exceeded 93.0% for all tested thresholds. Furthermore, as the threshold was relaxed from 3% to 10%, the proportion of Persistent zones systematically increased from 72.2% to 84.9%, while the proportion of Temporal-only zones correspondingly decreased. These findings indicate that the identified spatiotemporal priority structure is fundamentally robust and is not highly sensitive to the specific percentile choice.

5. Discussion

5.1. Multi-Hazard Integration: Beyond Single-Hazard Assessment

This study demonstrates that integrating seismic amplification susceptibility with flood hazard and time-varying population alters spatial exposure prioritization beyond single-hazard assessments. The multiplicative formulation implements a co-occurrence principle, whereby elevated multi-hazard exposure priority is identified only where unfavorable hazard conditions and population exposure co-occur.

Comparison between flood-only prioritization and the integrated multi-hazard framework showed substantial spatial overlap (Figure 8). This concordance indicates that flood hazard remains a dominant driver of urban risk patterns in Seoul. However, the divergent priority zones revealed meaningful spatial differences introduced by multi-hazard integration.

In particular, areas characterized by moderate flood hazard but unfavorable seismic site conditions emerged as integrated priorities, whereas some high-flood areas with relatively favorable seismic conditions exhibited reduced priority. These differences demonstrate that multi-hazard integration refines relative spatial prioritization by incorporating hazard co-location effects rather than merely reproducing flood-only prioritization.

5.2. Temporal Population Dynamics and Exposure Heterogeneity

Integration of dynamic living population data revealed that exposure-oriented multi-hazard exposure priority patterns vary systematically across the daily cycle. Even under identical hazard conditions, exposed population magnitude and spatial distribution differed markedly between daytime and nighttime, challenging conventional assessments based on static or residential population data.

In Day-peak zones, weekday daytime populations exceeded nighttime levels by a factor of 3.3 (204,000 vs. 61,000), reflecting the systematic absence of transient populations from residential registration data. As a result, static population-based assessments underestimate exposure during active daytime periods in these areas.

In contrast, Night-peak zones showed nighttime-dominant exposure patterns (167,000 vs. 115,000; ratio = 0.69), reflecting a residential population concentration that is more consistently captured in conventional planning frameworks. Persistent zones, while maintaining high-priority status across both periods, also exhibited non-negligible day–night variation (ratio = 1.17), indicating that even stable priority areas experience meaningful temporal fluctuations in exposure.

These results show that static exposure assessments assume temporally uniform population distributions, whereas observed day–night differentials reveal systematic temporal variability. Incorporating time-specific exposure profiles is therefore essential for accurate spatiotemporal exposure assessment.

5.3. Validation and Robustness of the Framework

Although the framework produces a relative exposure priority index rather than a predictive probabilistic risk model, the reliability of the results is supported at two lev-

els. At the component level, the seismic amplification susceptibility index was derived from 22,499 borehole records using ordinary kriging (RMSE = 189.85 m/s), providing spatially continuous estimates with quantified interpolation uncertainty. The flood hazard index, constructed from 41,980 flood trace polygons (2010–2024), was compared against district-level historical damage and casualty records, yielding statistically significant correlations ($p < 0.01$). The spatial pattern of nighttime dynamic living population showed strong spatial consistency with registered residential population density, supporting the representativeness of the mobile-based estimates.

At the result level, sensitivity analysis across priority thresholds of 3–10% yielded pattern concordance exceeding 93% (Table 4), confirming that the Persistent, Day-peak, and Night-peak classification is robust to threshold selection. The remaining 11% of the divergence between single- and multi-hazard rankings reflects systematic refinement from seismic site condition integration. These validation results support the analytical reliability of the spatiotemporal priority structure presented in Sections 5.1 and 5.2.

5.4. Implications for Time-Adaptive Urban Risk Management

The classification of priority zones into Persistent, Day-peak, and Night-peak types provides spatially explicit evidence supporting time-adaptive urban resilience strategies. Operating at a 250 m grid resolution allows the framework to capture micro-scale temporal transitions within administrative districts—variations across blocks, corridors, and elevation zones that are not observable in district-level analyses. These spatial distinctions provide a practical basis for differentiating time-specific resilience strategies across urban environments.

Persistent zones, accounting for approximately 80% of priority areas, maintain elevated priority regardless of the daily cycle, reflecting the convergence of multi-hazard conditions with sustained population presence. These broadly exposed areas warrant continuous risk reduction efforts. Practical measures require macro-scale physical improvements. To mitigate pluvial flooding, this includes upgrading existing drainage networks and installing deep underground rainwater storage tunnels—a critical infrastructure need for Seoul's low-lying basins. Simultaneously, for seismic hazards, it is essential to provide active administrative and financial support for the seismic retrofitting of existing older structures that lack proper seismic design. These combined structural efforts must be accompanied by the stable and consistent allocation of emergency response resources.

Day-peak zones, representing approximately 10% of priority areas and largely overlapping Zone A, concentrate disproportionately large exposed populations during daytime hours despite limited spatial extent. Exposure management must address vulnerabilities associated with transient populations, such as unfamiliarity with evacuation routes, information asymmetry, and concentration within high-rise buildings and transportation hubs. The primary objective in these zones is to prevent cascading failures in urban functions; therefore, robust information dissemination, rigorous crowd management, and the assurance of system continuity are critical priorities.

Night-peak zones, comprising roughly 10% of priority areas and largely overlapping Zone B, exhibit elevated exposure during nighttime hours. These areas are characterized by passive populations, including sleeping residents, older adults, and mobility-impaired individuals. Preparedness in these zones should prioritize life-saving response capacity. Crucial measures include installing high-decibel localized siren networks that do not rely solely on personal mobile devices, and pre-designating nearby accessible facilities, such as 24-h accessible shelters and local schools, as dedicated nighttime emergency shelters.

These patterns support a dual-response framework in which daytime strategies prioritize information flow and prevention of cascading failures in transportation and business

infrastructure, while nighttime strategies emphasize residential safety and rescue capacity (Table 5). Incorporating time-varying exposure into urban resilience planning enables exposure management aligned with the temporal dynamics of metropolitan activity.

Table 5. Time-adaptive management strategies by spatiotemporal transition type.

Feature	Daytime Protocol	Nighttime Protocol
Priority zones	Business districts, transport hubs (Day-peak)	Residential areas (Night-peak)
Exposed groups	Commuters, visitors, transient populations (Active)	Sleeping residents, mobility-impaired (Passive)
Primary vulnerabilities	Information asymmetry, unfamiliarity with routes, cascading traffic paralysis	Delayed awareness due to sleep state, evacuation constraints in older structures
Strategic focus	System continuity (Safe evacuation, cascading failure prevention)	Life-saving (Rapid alert, residential structural safety)

5.5. Limitations and Future Study

Despite its contributions, this study has several limitations. First, regarding spatial and methodological constraints, the framework operates at a 250 m grid resolution dictated by the native dynamic living population data. While optimal for distinguishing functional urban zones, it may smooth localized intra-block exposure peaks. Additionally, the spatial prioritization relies on a relative percentile-based definition (top 5%). Although sensitivity analyses (3–10% thresholds) demonstrated robust pattern concordance (>93%) and the percentile approach effectively identifies isolated high-priority locations that clustering methods (e.g., Gi* hotspot) might overlook, it remains a relative metric rather than an absolute risk threshold.

Second, the characterization of multi-hazard interactions involves certain simplifications. The current scope is limited to the spatial co-location of seismic amplification susceptibility and observed flood hazard. It does not fully account for cascading or secondary hazards, such as earthquake-triggered urban fires, earthquake-induced drainage failure or power outages amplifying flood impacts, which could intensify overall disaster impacts in a dense metropolis. Integrating cascading multi-hazard scenarios remains an important extension for future research.

Third, because the framework evaluates conditional exposure priority rather than probabilistic risk, the hazard components were treated as temporally invariant spatial indicators within a conditional scenario formulation. For flooding, the accumulated trace records inherently reflect the dominant summer monsoon season, but the present analysis does not explicitly model season-specific hazard probabilities. Although the diurnal scale was selected as the primary temporal dimension based on the population variability analysis presented in Section 3.3.3, and the broad seasonal consistency of the priority structure was additionally confirmed in Figure A1, coupling season-specific hazard probability models with seasonal dynamic population data would extend the present framework from conditional exposure prioritization to a time-resolved probabilistic risk assessment.

Finally, vulnerability was assumed to be spatially uniform to isolate physical exposure effects. Integrating spatially explicit social and structural vulnerability indicators, particularly regarding evacuation-constrained populations and building fragility, would further improve the differentiation between exposure prioritization and comprehensive risk quantification.

6. Conclusions

This study developed an observation-based multi-hazard exposure prioritization framework integrating seismic amplification susceptibility, flood hazard records, and time-varying populations at a 250 m grid resolution for Seoul, South Korea. Based on the UNDRR disaster risk framework, the analysis focused on the intersection of physical susceptibility and dynamic exposure across two distinct environmental hazards, without relying on probabilistic hazard modeling or spatially explicit vulnerability data. By combining observed susceptibility indicators with time-specific population estimates, the framework identifies not only where multi-hazard exposure priority concentrates but also when population exposure intensifies.

First, the integration of overlapping seismic amplification susceptibility and flood hazard revealed that flood hazard is the dominant driver of spatial priority patterns, with 89% of the top 5% priority zones coinciding between single-hazard and multi-hazard approaches. However, the remaining 11% diverged: areas with moderate flood hazard but unfavorable seismic site conditions were elevated to high priority under multi-hazard integration. Conversely, some high-flood areas with favorable seismic conditions were relatively deprioritized. This demonstrates that multi-hazard integration refines, rather than merely reinforces, single-hazard prioritization by accounting for hazard co-location.

Second, the incorporation of dynamic living population data revealed that identical hazard conditions generate markedly different priority patterns between daytime and nighttime. In business-oriented districts (Zone A), the weekday daytime priority index exceeded the nighttime value by a factor of 2.48. In residential districts (Zone B), the nighttime priority index was 2.02 times higher than the daytime value. Weekend patterns exhibited similar spatial tendencies with reduced magnitudes (Zone A: 1.62×; Zone B: 1.69×). These differentials indicate that static, census-based population data systematically mischaracterize priority during periods of peak urban activity.

Third, the high-resolution delineation of spatiotemporal priority zones classified 565 weekday high-priority grid cells into three distinct transition types: Persistent (79.4%), Day-peak (10.3%), and Night-peak (10.3%). Persistent zones, distributed across both Zone A and Zone B, contained approximately 1.34 million exposed persons during daytime and 1.14 million during nighttime, maintaining elevated priority regardless of the daily cycle. Day-peak zones, spatially concentrated along business corridors, exhibited the largest temporal asymmetry (day/night ratio = 3.35). Night-peak zones in residential areas showed the inverse pattern (ratio = 0.69). Sensitivity analysis confirmed that this spatiotemporal structure, defined at the top 5% threshold, is robust across alternative percentile thresholds (3–10%), with pattern concordance exceeding 93%.

The combined evidence indicates that multi-hazard exposure in metropolitan Seoul cannot be adequately characterized by static, single-time assessments. The observed spatiotemporal heterogeneity supports a shift toward time-adaptive management: Persistent zones warrant continuous macro-scale structural mitigation and resource allocation. Day-peak zones require daytime-focused measures (e.g., crowd management and mobile alerts) for transient populations, and Night-peak zones call for nighttime response capacity tailored to residential communities (e.g., localized sirens).

The modular framework structure supports broad transferability across different urban scales and disaster types. Driven by dynamic population grids, it can be adapted to cities of different scales where comparable population data are available. Furthermore, its flexible hazard layers allow easy adaptation to other environmental hazards, such as extreme heatwaves or coastal storm surges, providing a flexible foundation for time-adaptive urban resilience planning.

Author Contributions: Conceptualization, Y.L.; methodology, Y.L.; software, Y.L.; validation, Y.L. and J.K.; formal analysis, Y.L. and J.K.; investigation, Y.L. and J.K.; data curation, Y.L. and J.K.; writing—original draft preparation, Y.L. and J.K.; writing—review and editing, Y.L.; visualization, Y.L.; supervision, Y.L.; project administration, Y.L.; funding acquisition, Y.L. All authors have read and agreed to the published version of the manuscript.

Funding: This research was supported by a grant (2022-MOIS62-001(RS-2022-ND640011)) of National Disaster Risk Analysis and Management Technology in Earthquake funded by Ministry of Interior and Safety (MOIS, Republic of Korea).

Institutional Review Board Statement: Not applicable.

Informed Consent Statement: Not applicable.

Data Availability Statement: The data supporting the findings of this study are available from the corresponding author upon reasonable request.

Conflicts of Interest: The authors declare no conflicts of interest.

Appendix A

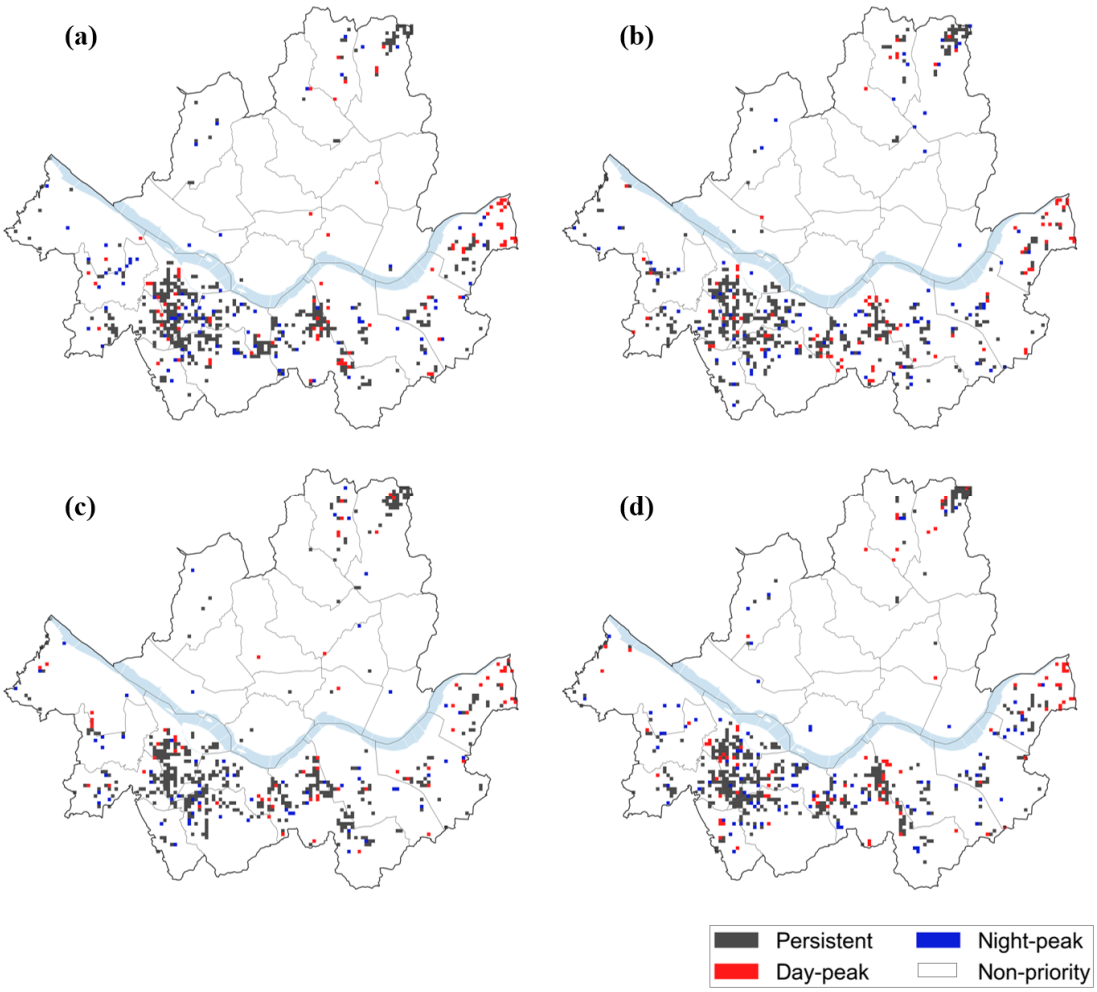


Figure A1. Seasonal variations in the weekday daytime multi-hazard exposure priority patterns across Seoul: (**a**) spring, (**b**) summer, (**c**) autumn, and (**d**) winter. Representative weekdays were selected from the month with the highest daytime dynamic living population in each season. The highlighted areas (black, red, and blue) represent the top 5% highest-priority zones.

References

1. Kumar, A.; Diksha; Pandey, A.C.; Khan, M.L. Urban risk and resilience to climate change and natural hazards: A perspective from million-plus cities on the Indian subcontinent. In *Techniques for Disaster Risk Management and Mitigation*; Srivastava, P.K., Singh, S.K., Mohanty, U.C., Murty, T., Eds.; John Wiley & Sons: Hoboken, NJ, USA, 2020; pp. 33–46.
2. Boni, M.P.; Faiella, A.; Gazzola, V.; Pergalani, F. A multi-hazard and multi-risk assessment methodological approach to support Civil Protection planning in wide areas. *Int. J. Disaster Risk Reduct.* **2025**, *119*, 105343. [CrossRef]
3. Kappes, M.S.; Gruber, K.; Frigerio, S.; Bell, R.; Keiler, M.; Glade, T. The MultiRISK platform: The technical concept and application of a regional-scale multihazard exposure analysis tool. *Geomorphology* **2012**, *151–152*, 139–155. [CrossRef]
4. Görüm, T.; Bozkurt, D.; Korup, O.; İstanbulluoğlu, E.; Şen, Ö.L.; Yılmaz, A.; Karabacak, F.; Lombardo, L.; Guan, B.; Tanyas, H. The 2023 Türkiye-Syria earthquake disaster was exacerbated by an atmospheric river. *Commun. Earth Environ.* **2025**, *6*, 151. [CrossRef]
5. Shen, S.V. The 2021 Henan flood increased citizen demand for government-led climate change adaptation in China. *Commun. Earth Environ.* **2025**, *6*, 730. [CrossRef]
6. Valente, M.; Del Prete, C.; Facci, G.; Martino, A.; Grilli, G.R.; Bravi, F.; Reno, C.; Ragazzoni, L. The 2023 floods in the Emilia-Romagna Region, Italy: A retrospective qualitative investigation into response strategies and criticalities. *Int. J. Disaster Risk Reduct.* **2025**, *116*, 105089. [CrossRef]
7. Quigley, M.; Duffy, B. Effects of earthquakes on flood hazards: A case study from Christchurch, New Zealand. *Geosciences* **2020**, *10*, 114. [CrossRef]
8. Bae, S.; Chang, H. Urbanization and floods in the Seoul Metropolitan area of South Korea: What old maps tell us. *Int. J. Disaster Risk Reduct.* **2019**, *37*, 101186. [CrossRef]
9. Daniell, J.E.; Schaefer, A.M.; Wenzel, F. Losses associated with secondary effects in earthquakes. *Front. Built Environ.* **2017**, *3*, 30. [CrossRef]
10. Hughes, M.W.; Quigley, M.; Van Ballegooy, S.; Deam, B.; Bradley, B.; Hart, D.; Measures, R. The sinking city: Earthquakes increase flood hazard in Christchurch, New Zealand. *GSA Today* **2015**, *25*, 4–10. [CrossRef]
11. De Ruiter, M.C.; Ward, P.J.; Daniell, J.E.; Aerts, J.C. A comparison of flood and earthquake vulnerability assessment indicators. *Nat. Hazards Earth Syst. Sci.* **2017**, *17*, 1231–1251. [CrossRef]
12. Kamat, R. Planning and managing earthquake and flood prone towns. *Stoch. Environ. Res. Risk Assess.* **2015**, *29*, 527–545. [CrossRef]
13. van Westen, C.; Hazarika, M.; Dahal, A.; Kshetri, T.; Shakya, A.; Nashrrullah, S. The RiskChanges tool for multi-hazard risk-informed planning at local government level. In Proceedings of the EGU General Assembly 2022, Vienna, Austria & Online, 23–27 May 2022.
14. Arrighi, C.; Tanganelli, M.; Cristofaro, M.; Cardinali, V.; Marra, A.; Castelli, F.; De Stefano, M. Multi-risk assessment in a historical city. *Nat. Hazards* **2023**, *119*, 1041–1072. [CrossRef]
15. White, C.J.; Adnan, M.S.G.; Arosio, M.; Buller, S.; Cha, Y.; Ciurean, R.; Crummy, J.M.; Duncan, M.; Gill, J.; Kennedy, C.; et al. Review article: Towards multi-hazard and multi-risk indicators—A review and recommendations for development and implementation. *Nat. Hazards Earth Syst. Sci.* **2025**, *25*, 4263–4281. [CrossRef]
16. Zscheischler, J.; Westra, S.; van den Hurk, B.J.J.M.; Seneviratne, S.I.; Ward, P.J.; Pitman, A.; AghaKouchak, A.; Bresch, D.N.; Leonard, M.; Wahl, T.; et al. Future climate risk from compound events. *Nat. Clim. Change* **2018**, *8*, 469–477. [CrossRef]
17. Tenerelli, P.; Gallego, J.F.; Ehrlich, D. Population density modelling in support of disaster risk assessment. *Int. J. Disaster Risk Reduct.* **2015**, *13*, 334–341. [CrossRef]
18. Yu, K.; Chouinard, L.E.; Rosset, P. Seismic vulnerability assessment for Montreal. *Georisk Assess. Manag. Risk Eng. Syst. Geohazards* **2016**, *10*, 164–178. [CrossRef]
19. Viavattene, C.; Jiménez, J.A.; Ferreira, O.; Priest, S.; Owen, D.; McCall, R. Selecting coastal hotspots to storm impacts at the regional scale: A Coastal Risk Assessment Framework. *Coast. Eng.* **2018**, *134*, 33–47. [CrossRef]
20. Geiß, C.; Maier, J.; So, E.; Schoepfer, E.; Harig, S.; Gómez Zapata, J.C.; Zhu, Y. Anticipating a risky future: Long short-term memory (LSTM) models for spatiotemporal extrapolation of population data in areas prone to earthquakes and tsunamis in Lima, Peru. *Nat. Hazards Earth Syst. Sci.* **2024**, *24*, 1051–1064. [CrossRef]
21. Malakar, M.; Malakar, S.; Hasan, M.S.U.; Rai, A.K.; Kannaujiya, V.K. Seismic risk assessment using integrated MCDM method in West Bengal, India. *Evol. Earth* **2024**, *2*, 100036. [CrossRef]
22. Rahimi, F.; Sadeghi Niaraki, A.; Ghodousi, M.; Choi, S.M. Spatial-temporal modeling of urban resilience and risk to earthquakes. *Sci. Rep.* **2025**, *15*, 8321. [CrossRef]
23. Zhang, N.; Huang, H.; Duarte, M.; Zhang, J.J. Dynamic population flow based risk analysis of infectious disease propagation in a metropolis. *Environ. Int.* **2016**, *94*, 369–379. [CrossRef]
24. Lee, Y.; Yoo, J.-K. High-Resolution Seismic Susceptibility Assessment Integrating Vulnerability and Exposure Indicators: Application to Seoul. *Appl. Sci.* **2025**, *15*, 11942. [CrossRef]

25. Zhu, Y.; Wang, J.; Manoli, G.; Zhang, Y.; Chi, D.; Meili, N.; Qiu, Y.; Lin, G.-S.; Tan, P.Y.; Burlando, P.; et al. Influence of urban form and function on daytime-nighttime population differences and hazard risk assessments. *npj Urban Sustain.* **2025**, *5*, 91. [CrossRef]
26. Depietri, Y.; Dahal, K.; McPhearson, T. Multi-hazard risks in New York City. *Nat. Hazards Earth Syst. Sci.* **2018**, *18*, 3363–3381. [CrossRef]
27. Ministry of the Interior and Safety. *Statistical Yearbook of Natural Disaster 2024*; Ministry of the Interior and Safety (MOIS): Sejong, Republic of Korea, 2025.
28. Sun, C.-G. Applications of a GIS-based geotechnical tool to assess spatial earthquake hazards in an urban area. *Environ. Earth Sci.* **2011**, *65*, 1987–2001. [CrossRef]
29. Aaqib, M.; Park, D.; Lee, Y.G.; Pervaiz, U. Development of site classification system and seismic site coefficients for Korea. *J. Earthq. Eng.* **2022**, *26*, 8257–8279. [CrossRef]
30. United Nations Office for Disaster Risk Reduction. *Sendai Framework for Disaster Risk Reduction 2015–2030*; United Nations Office for Disaster Risk Reduction (UNDRR): Geneva, Switzerland, 2015.
31. Yun, H.S.; Lee, J.Y.; Yang, D.Y.; Hong, S.S. Areal distribution ratio of rock type with geologic ages in the Gyeonggi-Seoul-Incheon areas. *J. Petrol. Soc. Korea* **2007**, *16*, 208–216.
32. Choi, J.H.; Ko, K.; Gihm, Y.S.; Cho, C.S.; Lee, H.; Song, S.G.; Bang, E.S.; Lee, H.J.; Bae, H.K.; Kim, S.W. Surface deformations and rupture processes associated with the 2017 M w 5.4 Pohang, Korea, earthquake. *Bull. Seismol. Soc. Am.* **2019**, *109*, 756–769. [CrossRef]
33. Seoul Metropolitan Government. *2040 Seoul Urban Master Plan*; Seoul Metropolitan Government (SMG): Seoul, Republic of Korea, 2023.
34. Korean Statistical Information Service. Resident registration population statistics. Available online: https://kosis.kr (accessed on 3 December 2025).
35. Aubrecht, C.; Meier, P.; Taubenböck, H. Speeding up the clock in remote sensing: Identifying the 'black spots' in exposure dynamics by capitalizing on the full spectrum of joint high spatial and temporal resolution. *Nat. Hazards* **2017**, *86*, 177–182. [CrossRef]
36. Lee, K.; Yang, W.-S. Historical seismicity of Korea. *Bull. Seismol. Soc. Am.* **2006**, *96*, 846–855. [CrossRef]
37. Han, J.; Nur, A.S.; Syifa, M.; Ha, M.; Lee, C.-W.; Lee, K.-Y. Improvement of Earthquake Risk Awareness and Seismic Literacy of Korean Citizens through Earthquake Vulnerability Map from the 2017 Pohang Earthquake, South Korea. *Remote Sens.* **2021**, *13*, 1365. [CrossRef]
38. Kim, H.S.; Sun, C.G.; Lee, M.G.; Cho, H.I. Multivariate geotechnical zonation of seismic site effects with clustering-blended model for a city area, South Korea. *Eng. Geol.* **2021**, *294*, 106365. [CrossRef]
39. Kim, B.; Ji, Y.; Kim, M.; Lee, Y.-J.; Kang, H.; Yun, N.-R.; Kim, H.; Lee, J. Building Damage Caused by the 2017 M5.4 Pohang, South Korea, Earthquake, and Effects of Ground Conditions. *J. Earthq. Eng.* **2022**, *26*, 3054–3072. [CrossRef]
40. Kim, H.-A.; Ho, C.-H.; Kim, J.; Seo, E.-K.; Park, S.K. Observational study of a quasi-stationary mesoscale convective system during extreme rainfall on 8 August 2022 in Korea. *Atmos. Res.* **2025**, *325*, 108159. [CrossRef]
41. Seoul Metropolitan Government. Seoul Open Data Plaza—Flood Trace Data. Available online: https://data.seoul.go.kr/dataList/OA-15636/F/1/datasetView.do (accessed on 31 October 2025).
42. Lee, S.; Choi, Y.; Ji, J.; Lee, E.; Yi, S.; Yi, J. Flood Vulnerability Assessment of an Urban Area: A Case Study in Seoul, South Korea. *Water* **2023**, *15*, 1979. [CrossRef]
43. Korea Meteorological Administration. Weather Nuri—Earthquake Records. Available online: https://www.weather.go.kr/w/eqk-vol/search/korea.do (accessed on 31 October 2025).
44. Lee, Y.; Lee, Y.-G.; Park, D. Geotechnical data based seismic microzonation in Seoul using region-specific and code-based site amplification models. *Bull. Earthq. Eng.* **2024**, *22*, 2375–2403. [CrossRef]
45. Ministry of Land, Infrastructure and Transport. National Spatial Data Infrastructure Portal. Available online: https://www.geoinfo.or.kr/ (accessed on 16 April 2023).
46. Ahn, J.-K.; Kwak, D.Y.; Kim, H.-S. Estimating VS30 at Korean Peninsular seismic observatory stations using HVSR of event records. *Soil Dyn. Earthq. Eng.* **2021**, *146*, 106650. [CrossRef]
47. Brandenberg, S.J.; Bellana, N.; Shantz, T. Shear wave velocity as function of standard penetration test resistance and vertical effective stress at California bridge sites. *Soil Dyn. Earthq. Eng.* **2010**, *30*, 1026–1035. [CrossRef]
48. Oliveira, L.; Teves-Costa, P.; Pinto, C.; Gomes, R.C.; Almeida, I.M.; Ferreira, C.; Pereira, T.; Sotto-Mayor, M. Seismic microzonation based on large geotechnical database: Application to Lisbon. *Eng. Geol.* **2020**, *265*, 105417. [CrossRef]
49. Baek, W.-H.; Chung, E.-S.; Choi, J.-S.; Ahn, J.-K. Determining Maintenance Project Priority Based on Disaster Risk Assessment: Case of TOPSIS Applications. *J. Korean Soc. Hazard Mitig.* **2022**, *22*, 255–261. [CrossRef]
50. Seoul Metropolitan Government. Seoul Open Data Plaza—Dynamic Living Population. Available online: https://data.seoul.go.kr/dataList/OA-22784/S/1/datasetView.do (accessed on 31 December 2025).
51. Pew Research Center. 8 Charts on Technology Use Around the World. Available online: https://www.pewresearch.org/short-reads/2024/02/05/8-charts-on-technology-use-around-the-world/ (accessed on 2 January 2026).

52. Seoul Metropolitan Government; KT. *Development of Seoul De Facto Population Estimation Model*; Seoul Metropolitan Government (SMG): Seoul, Republic of Korea, 2018.
53. Gallina, V.; Torresan, S.; Critto, A.; Sperotto, A.; Glade, T.; Marcomini, A. A review of multi-risk methodologies for natural hazards: Consequences and challenges for a climate change impact assessment. *J. Environ. Manag.* **2016**, *168*, 123–132. [CrossRef] [PubMed]
54. Building Seismic Safety Council (BSSC). *NEHRP Recommended Seismic Provisions for New Buildings and Other Structures*; Rep. No. P-1050-1; Federal Emergency Management Agency (FEMA): Washington, DC, USA, 2015.
55. Sun, C.G.; Cho, C.S.; Son, M.; Shin, J.S. Correlations between shear wave velocity and In-situ penetration test results for Korean soil deposits. *Pure Appl. Geophys.* **2013**, *170*, 271–281. [CrossRef]

Disclaimer/Publisher's Note: The statements, opinions and data contained in all publications are solely those of the individual author(s) and contributor(s) and not of MDPI and/or the editor(s). MDPI and/or the editor(s) disclaim responsibility for any injury to people or property resulting from any ideas, methods, instructions or products referred to in the content.